Experimental analysis and damage modeling of the shear-out failure mode of a 3D woven composite lug

Cécile Garcia, Antoine Hurmane, François-Xavier Irisarri, Frédéric Laurin, Sylvain Leclercq, Rodrigue Desmorat

Experimental analysis and damage modeling of the shear-out failure mode of a 3D woven composite lug

Cécile Garcia[a,b,c], Antoine Hurmane[a], François-Xavier Irisarri[a], Frédéric Laurin[a], Sylvain Leclercq[b], Rodrigue Desmorat[c]

[a] *ONERA, DMAS, Université Paris-Saclay F-92320 Châtillon, France*
[b] *Safran Landing Systems, Inovel Parc Sud 78140 Vélizy-Villacoublay, France*
[c] *Université Paris-Saclay, ENS Paris-Saclay, CNRS, LMT - Laboratoire de Mécanique et Technologie, 94235, Cachan, France*

Abstract

This study focuses on the shear-out failure mode of a 3D-woven composite lug. The damage scenario leading to the failure is analyzed based on a tensile test on a lug. The shear-out failure of the lug is shown to be driven by matrix damages generated by in-plane shear. No yarn failure is observed. A matrix damage model is proposed to capture the shear-out failure of the lug. This model combines the Onera Damage Model for Polymer Matrix Composite (ODM-PMC) with a Mazars-like damage evolution law. A special attention is paid for the transition between both evolution laws, in order to ensure the continuity of the damage evolution. The model is implemented into the commercial Abaqus Standard finite element (FE) software. A 3D FE analysis of the shear-out failure of the lug is performed. The simulation is able to reproduce the load plateau observed in the global behavior of the lug as well as the specific matrix damage patterns.

Keywords:

3D Woven Composite, Mechanical joint, Shear-out failure, Damage model,

1. Introduction

Lugs are often used in aircraft structures to connect structural elements, transmit motions and transfer loads. For example, systems of struts connected by lugs are used to fold in and out modern airliner landing gears. The lugs also transfer the load from the wheels to the airliner structure during take off and landing. Thus, lugs can be highly loaded primary structures, critical to structural integrity and flight safety. Landing gear lugs are usually made of metallic materials. Composite lugs promise significant weight savings. Landing gear systems are vulnerable to impact of debris during taxi. Consequently, 3D woven composite materials are interesting candidate materials for innovative composite lug designs for landing gears.

From a design viewpoint, a lug can be considered as a special case of pinned or bolted joint. Focusing on the composite part in the joint, the main failure modes are net section tensile failure, bearing failure and shear-out failure. The complexity of the design problem results from the competition between these three failure modes. Although metallic and composite joints present similar failure modes from a phenomenological point of view, the physical mechanisms involved are fundamentally different. The sizing of joints [1, 2] or lugs [3, 4] in industry is usually based on elastic stress analysis and semi-empirical strength analysis methods. Such methods are fast and well-suited for trade-off studies and design optimization. Nonetheless their domains of validity are generally very limited, making it necessary to build large and expansive experimental databases. Therefore the use of numerical

methods for the detailed analysis of the joint behavior and failure, most often finite elements, is now widely accepted.

The main influential parameters on the failure of composite joints have been known since the 1970's based on large experimental studies on composite laminates by Collings [5] and Hart-Smith [6]. Material anisotropy and joint geometrical parameters drive the competition between the failure modes. Net-tension failure appears in the case of small width joints and low proportion of longitudinal fiber reinforcements. Kassapoglou and Townsend [4] proposed a method to predict the failure of laminated composite lugs failing in tension. Shear-out failure appears for joints with short end-distance and low out-of-axis material reinforcements. With high end-distance-to-diameter and width-to-diameter ratios appears the bearing failure mode which corresponds to the ovalization of the hole in the loading direction due to the crushing of the material by the loading axis. The analysis and modeling of the bearing failure in composite laminates has driven the attention of many researchers during the last decades [6, 5, 7, 8, 9, 10, 11, 12]. Much less research effort has been dedicated to tensile and shear-out failure modes. On the one hand, tensile failure of the joint seems very similar to the tensile failure of open-hole plates. On the other hand, shear-out failure can be easily avoided in typical aircraft applications through appropriate sizing of the joint, even if this is not the case for all applications [13].

The 3D woven composite materials, and, a fortiori, the 3D woven composite lugs are much more recent and less studied topics. McClain and Timoshchuk [14] performed an experimental study of the bearing behavior of several 3D woven composites with different preform types of weaves. Warren

et al. [15] studied the bearing failure of 3D woven composite materials in different joint configurations and material orientations. The authors subsequently proposed [16] a three-dimensional progressive damage model to capture the damage onset and beginning of propagation. The authors predicted the bearing failure of a single-bolt double-shear joint using a finite element model based on a voxelized mescospic representation of the woven material. Finally, Mounien et al. [17] gave a detailed description of the scenario of the local damages leading to bearing failure of a 3D woven composite and showed that the bearing strength is a slightly decreasing nonlinear function of the square root of the diameter-to-thickness ratio. However all these studies focus on classical joint geometries. In this study, it is shown that the shear-out failure mode can be critical for monolithic 3D woven composite lugs, due to the lug geometry and to the lack of off-axis fibers. The experimental results show the development of a stable load plateau during shear tear-out failure of the lug. The failure scenario is derived from the experimental analysis and a 3D progressive damage model is proposed to capture the shear-out failure.

A load plateau is often modeled by elasto-plasticity when no loss of stiffness is observed [18]. Elasto-plasticity can be coupled with damage, but it increases the modeling complexity since material parameters are then introduced for both the damage evolution and the permanent/anelastic strains evolution [19, 20, 21]. Internal sliding and friction theory can also be used, but a multiscale analysis accounting for the anisotropic microstructure degradation is needed [22, 23, 24, 25], which is difficult to perform for woven composites [26]. Another modeling possibility is to consider both loss of stiffness and permanent strains as governed by damage directly at the Representative

Volume Element (RVE) scale [27, 28]. This is this last approach that will be followed. In section 4, it will be combined with Mazars' damage evolution law —initially proposed for concrete [29]— which accounts for a plateau after stress softening in tension.

2. Experimental analysis

2.1. Experimental set-up

The material considered in this study is a 3D woven composite developed by Safran Group. It is made of carbon fiber yarns (48 K) and epoxy matrix. The material is highly unbalanced with a higher yarn fiber volume fraction in the warp direction than in the weft direction. The weaving was specifically designed to prevent large delamination cracks after impact, and therefore providing a good impact resistance. Although its architecture is confidential, a generic architecture of an unbalanced 3D woven composite material is provided in Figure 1. The RVE is markedly larger than those of other composite materials.

[Figure 1 about here]

A specific test set-up was developed to perform a double-lap bearing test on the 3D woven composite lug. The dimensions of the lug are shown in Figure 2. The lug is directly machined from a 3D woven composite plate, so that the material orientation is uniform over the part. The warp direction is aligned with length of the specimen, in the y-axis direction. The hole diameter D is 50 mm. The difference between the loading axis diameter and the hole diameter is inferior to 0.03 mm. The outer diameter of the lug D_{ext} is 150 mm. Considering that the material presents no out-of-axes fiber

reinforcement and the low ratio between the outer diameter and the inner diameter of the lug $D_{ext}/D = 3$, the lug is prone to shear-out failure. For this specific configuration, only one specimen has been tested.

[Figure 2 about here]

The test was performed on a hydraulic machine with a maximum capacity of 500 kN. The test was displacement-controlled with a loading rate of 0.1 mm/min so that the loading conditions can be considered as quasi-static. The experimental set-up is reported in Figure 3. A solid axis made of steel is used to transfer the load to the lug. The loading axis is set to the upper clamping jaw of the test machine by means of a steel set-up specially devised for this test. During the test, the upper clamping jaw is fixed. The lower part of the lug is directly fixed in the lower jaw, which is mobile.

[Figure 3 about here]

With the aim of establishing a precise damage scenario, the test was multi-instrumented. In particular, the steel set-up was designed to include a window, thus enabling the observation of the surface of the nose of the lug, where the failure is expected. The monitoring of the 3D displacement fields on the surface of the lug through the observation window is performed with a system of stereo digitial image correlation (DIC). Images were acquired with 0.25 Hz acquisition frequency using digital 12-bit CCD cameras system, with a 2000*2000 pixels resolution. They were post-processed with the commercial software *Vic3D*©. A Nano30 acoustic emission (AE) sensor was located at the bottom of the lug to monitor the succession of local damage events. The recorded data were processed using *AEWin* which is part of the MISTRAS software. The threshold for acoustic emission is set to 47 dB to

avoid recording machine noises. Finally, in addition to the force and the displacement measurements provided by the machine, a LVDT sensor is used to measure the relative displacement between the loading axis and mobile jaw of the machine.

2.2. Failure scenario

The global behavior of the lug under tensile loading is reported in Figure 4. On the same graph is superimposed the cumulative acoustic energy which provides information on damage evolution. The epipolar error given by the software *Vic3D* [30] is used to monitor the crack emergence on the surface of the sample. After initial clearance recovery, the specimen response can be described in three principal phases. In a first phase, the global response is quasi-linear until the first significant acoustic events (at about 70% of the maximal load). The second phase is characterized by the development of matrix cracking parallel to the loading direction. The cracks propagate from the loaded boundary of the hole and along two symmetrical planes on the left and right sides of the hole, that are locally highly subjected to in-plane shear stress. The shear-out planes are coplanar to the (Y,Z)-plane. They are not tangent to the hole boundary but intersect the hole boundary at points located at about $\pm 70\%$ with respect the loading direction. The cracks propagate progressively until crossing the whole ligament. The global behavior becomes increasingly non-linear with the crack propagation until reaching a stable load plateau that approximately corresponds to the maximal load.

The load plateau characterizes the third phase of the observed behavior. The material of the nose of the lug that is located in between the two shear-

out planes is progressively pushed out. The crack density increases gradually on both sides of the shear-out planes. At the end of the test, the damaged area extends over several millimeters on both sides of the shear-out planes. No damage is observed in the portion of the lug that is pushed-out. The observation of the failure pattern presented that the warp yarns are debonded near the shear-out planes, what can be clearly observed at the extremity of the lug in Figure 5.b. Figure 5.a shows a view of the mid-thickness of the specimen obtained thanks to X-Ray tomography. The tomography was performed after the test at Safran with a 30 μm voxel resolution. The figure shows the deformation of the weft yarns that wave when crossing the shear-out plane. The weft yarns are not broken although they bend locally. Matrix cracking can be observed in a region that extends over one or two warp yarns on each side of the shear plane. The corresponding warp yarns are debonded on their total length throughout the ligament. The regular evolution of the acoustic cumulative energy corroborates that matrix damages develop during the plateau. No fiber yarn failure has been detected in the lug. Therefore, the only damage mechanism involved in the shear-out failure of the lug is matrix cracking.

During unloading, no significant acoustic event is recorded. The cumulative acoustic energy remains thus constant, meaning that damages do not evolve while unloading. The important hysteresis that can be seen in Figure 4 is probably related to the viscosity of the matrix. Friction between the debonded warp yarns and the surrounding matrix could also play a non negligible role in the residual displacement measured after unloading. As a matter of fact, the debonded warp yarns do not get their initial position back,

as shown in Figure 5.b. However, the matrix damage creation under in-plane shear clearly plays a first order role in the shear-out failure mode. Both DIC and AE show the development of significant matrix damages, first during the non-linear phase that precedes the plateau and then during the plateau itself. Thus, it can be assumed from this test that the shear-out failure mode of the 3D-woven composite lug is mostly driven by matrix damage creation under local in-plane shear loading. For that reason, it has been decided to depict the behavior of the lug by means of a damage model.

[Figure 4 about here]

[Figure 5 about here]

3. Matrix damage modeling for 3D woven composite materials

The choice was made to use the Onera Damage Model for Polymer Matrix Composite (ODM-PMC) which is a continuum damage model developed for 3D-woven composites with polymer matrix. ODM-PMC is a macroscopic model devised to simulate damage evolution in large composite structures. The model is thermodynamically consistent. It takes into account the contributions of different non-linearity sources on the material compliance, namely the effects of the viscosity of the matrix, matrix cracking and progressive fiber yarn failure, so that the behavior writes:

$$\boldsymbol{\sigma} = \underline{\underline{C}}^{eff} : \boldsymbol{\varepsilon}, \tag{1}$$

with $\underline{\underline{C}}^{eff} = (\underline{\underline{S}}^{eff})^{-1}$ the effective (damaged) stiffness tensor.

It has been demonstrated that ODM-PMC is able to effectively predict the material behavior up to failure for monotonic static loadings in compression

[31] and under impacts [32]. A global description of the ODM-PMC model can be found in [31].

In this paper, considering the damage and failure scenario described in Section 2.2, it has been chosen to focus on the matrix cracking only. For the sake of simplicity, all other non-linear mechanisms are deactivated in the following. After a careful analysis of CT-Scan results, we choose to neglect the damage in thickness direction, which seems to be secondary for the considered shear-out failure mode. Two scalar damage variables d_1 and d_2 are considered and describe the effect of matrix cracks in respectively the warp and weft directions. The driving forces of these damage mechanisms, noted y_1 and y_2, are given by [33, 34]:

$$\begin{cases} y_1 = \frac{1}{2}\Big(C^0_{11}(\varepsilon^{d_1+}_{11})^2 + a_{16}C^0_{66}(\varepsilon^{d_1+}_{12})^2 + a_{15}C^0_{55}(\varepsilon^{d_1+}_{13})^2\Big) \\ y_2 = \frac{1}{2}\Big(C^0_{22}(\varepsilon^{d_2+}_{22})^2 + a_{26}C^0_{66}(\varepsilon^{d_2+}_{12})^2 + a_{24}C^0_{44}(\varepsilon^{d_2+}_{23})^2\Big) \end{cases} \tag{2}$$

In these equations, C^0_{ij} are the components of the initial elastic orthotropic rigidity tensor using Voigt form:

$$\underline{\underline{C}}^0 = (\underline{\underline{S}}^0)^{-1} = \begin{bmatrix} \frac{1}{E_1} & -\frac{\nu_{12}}{E_1} & -\frac{\nu_{13}}{E_1} & 0 & 0 & 0 \\ -\frac{\nu_{21}}{E_2} & \frac{1}{E_2} & -\frac{\nu_{23}}{E_2} & 0 & 0 & 0 \\ -\frac{\nu_{31}}{E_3} & -\frac{\nu_{32}}{E_3} & \frac{1}{E_3} & 0 & 0 & 0 \\ 0 & 0 & 0 & \frac{1}{G_{23}} & 0 & 0 \\ 0 & 0 & 0 & 0 & \frac{1}{G_{31}} & 0 \\ 0 & 0 & 0 & 0 & 0 & \frac{1}{G_{12}} \end{bmatrix}. \tag{3}$$

The material coefficients a_{16}, a_{15}, a_{26}, a_{24} quantify the influence of the different shear strains on the onset of damage.

In equations (2), $\boldsymbol{\varepsilon}^{d_1+} = (\boldsymbol{\varepsilon}^{d_1})^+$ and $\boldsymbol{\varepsilon}^{d_2+} = (\boldsymbol{\varepsilon}^{d_2})^+$ are the positive strains tensors defined with respect to

$$\boldsymbol{\varepsilon}^{d_1} = \begin{bmatrix} \varepsilon_{11} & \varepsilon_{12} & \varepsilon_{13} \\ \varepsilon_{12} & 0 & 0 \\ \varepsilon_{13} & 0 & 0 \end{bmatrix}, \qquad \boldsymbol{\varepsilon}^{d_2} = \begin{bmatrix} 0 & \varepsilon_{12} & 0 \\ \varepsilon_{12} & \varepsilon_{22} & \varepsilon_{32} \\ 0 & \varepsilon_{32} & 0 \end{bmatrix}. \tag{4}$$

according to the degradation mechanisms respectively represented by d_1 and d_2. For more details, refer to Appendix A.

The evolution laws for the damages d_i ($i = 1$ or 2) are given by equation (5), where $\langle \bullet \rangle$ are the Macauley brackets, means the positive part of a scalar, defined as $\langle x \rangle = \max(0, x)$:

$$g(y_i) = d_i^{sat}\left(1 - exp\left[-\left(\frac{\langle \sqrt{y_i} - \sqrt{y_{i0}} \rangle}{\sqrt{y_{ic}}}\right)^{p_i}\right]\right). \tag{5}$$

In order to prevent a decrease of damage, the upper bound of this quantity is considered:

$$d_i(t) = \sup_{t \leq \tau} g(y_i(\tau)) \in \left[0, d_i^{sat}\right]. \tag{6}$$

The damage d_i activates at the damage threshold y_{i0}; d_i can increase until a saturation value equal to d_i^{sat}, that corresponds to a residual stiffness at high strain levels in the corresponding reinforcement direction due to the presence of yarn reinforcement. Two parameters drive the damage evolution law, namely y_{ic} and p_i. To sum up, the 4 damage parameters are y_{i0}, y_{ic}, p_i and d_i^{sat}, with $i = 1$ or 2, and must be identified.

The effect of the matrix damages are taken into account through the increase of the effective compliance tensor $\underline{\underline{S}}^{eff}$:

$$\underline{\underline{S}}^{eff} = (\underline{\underline{C}}^{eff})^{-1} = \underline{\underline{S}}_0 + d_1\underline{\underline{H}}_1 + d_2\underline{\underline{H}}_2 \tag{7}$$

The value of the damage d_i (as well as its saturation value d_i^{sat}) may be larger than 1 because d_1 and d_2 increase the stiffness, and d_i^{sat} could asymptotically tend to infinity. A more classical damage variable D_i, upper bounded by 1, may be alternatively defined as:

$$D_i = \frac{d_i}{1 + d_i} \in [0, 1] \,. \tag{8}$$

Permanent strains are neglected here. The effect tensors $\underline{\underline{H_i}}$ impact differently the initial compliance $\underline{\underline{S}}_0$ depending on the material direction:

$$\begin{aligned}
\underline{\underline{H_1}} &= \begin{bmatrix}
h_{11}S_{11}^0 & 0 & 0 & 0 & 0 & 0 \\
0 & 0 & 0 & 0 & 0 & 0 \\
0 & 0 & 0 & 0 & 0 & 0 \\
0 & 0 & 0 & 0 & 0 & 0 \\
0 & 0 & 0 & 0 & h_{55}S_{55}^0 & 0 \\
0 & 0 & 0 & 0 & 0 & h_{66}^1 S_{66}^0
\end{bmatrix}, \\
\underline{\underline{H_2}} &= \begin{bmatrix}
0 & 0 & 0 & 0 & 0 & 0 \\
0 & h_{22}S_{22}^0 & 0 & 0 & 0 & 0 \\
0 & 0 & 0 & 0 & 0 & 0 \\
0 & 0 & 0 & h_{44}S_{44}^0 & 0 & 0 \\
0 & 0 & 0 & 0 & 0 & 0 \\
0 & 0 & 0 & 0 & 0 & h_{66}^2 S_{66}^0
\end{bmatrix}.
\end{aligned} \tag{9}$$

where S_{ij}^0 are components of the initial compliance tensor, and h_{ij} are factors that weight the effect of damage on the compliance tensor in the different directions.

The local behavior modeled with ODM-PMC is illustrated in Figure 6. The black points correspond to tensile test data performed in different mate-

rial orientations at Onera whereas the blue curves are obtained using ODM-PMC. The experimental global behaviors observed in the 0°and 90°directions are well captured by the model. In the weft direction, the necessity of introducing a saturation is clearly observed. The good match between the experimental data and the model for the 45°off-axis tensile test validates the model for low in-plane shear strain values. The experimental response for pure in-plane shear loading is unknown since there is no simple test on elementary 3D woven composite specimen capable of creating a pure in-plane shear stress state.

[Figure 6 about here]

4. Continuous damage modeling of a stress plateau

The challenge here is to determine the material in-plane shear behavior that is required to capture the global shear-out failure of the lug. It is clear from Figure 6 that the ODM-PMC satisfactorily captures the in-plane behavior of the material for low in-plane shear strain values. Thus, the model is able to capture the effect of the first matrix cracks that are observed in Figure 4 at the beginning of the non-linear phase prior to the shear-out plateau. To depict the load plateau observed in the global behavior of the lug, it could be considered reasonably that a plateau is also required at the material scale for pure shear loading. Hence, the local material behavior that has to be described for a pure in-plane shear loading should present four distinct phases illustrated in Figure 7. The first two phases can be accurately be described by ODM-PMC. An almost linear behavior phase is followed by damage creation and propagation for low in-plane shear strain

values (phase two). The third phase corresponds to the transition towards the stress plateau (phase four), that corresponds to the steady development of matrix cracking for high in-plane shear strain values. The extent of the transition phase depends on the ratio between the maximal value τ_{12}^{max} of the in-plane shear stress over whole history, up to current time, and the value $\tau_{12}^{plateau}$ of the stress plateau. Since τ_{12}^{max} is necessarily superior or equal to $\tau_{12}^{plateau}$, the transition phase corresponds to a softening behavior.

[Figure 7 about here]

4.1. The Mazars damage model

Mazars [29] developed a model to describe the behavior of isotropic concrete materials which presents a plateau for high strain levels. The model uses the concept of effective stress $\tilde{\boldsymbol{\sigma}}$ for initially isotropic materials:

$$\tilde{\boldsymbol{\sigma}} = \frac{\boldsymbol{\sigma}}{1-D} = \underline{\underline{C}}^0 : \boldsymbol{\varepsilon}, \tag{10}$$

where D is the standard damage variable evolving between 0 and 1 and $\underline{\underline{C}}^0$ the initial isotropic compliance. In this model, it is assumed that the damage is isotropic, hence a unique damage variable is considered.

The damage evolution law is given by:

$$D = 1 - \frac{(1-A)\varepsilon_0}{\varepsilon_{eq}^{max}} - A\exp[-B\langle\varepsilon_{eq}^{max} - \varepsilon_0\rangle], \tag{11}$$

with $\varepsilon_{eq}^{max}(t) = \sup_{t\leq\tau}\varepsilon_{eq}(\tau)$ the maximum value over whole history, up to current time, of the considered equivalent strain ε_{eq}. In this equation, ε_0 is the damage threshold in terms of strain, ε_{eq} is Mazars equivalent strain computed from the principal strains ε_I, ε_{II} and ε_{III}:

$$\varepsilon_{eq} = \sqrt{\langle\varepsilon_I\rangle^2 + \langle\varepsilon_{II}\rangle^2 + \langle\varepsilon_{III}\rangle^2}. \tag{12}$$

For illustration matters, uniaxial tension is considered in the following, Mazars equivalent strain ε_{eq} being equal to the uniaxial strain $\varepsilon = \varepsilon_{11}$. A and B are the two damage parameters of the model. Their influence is illustrated in Figure 8. The parameter A monitors the plateau position and the parameter B drives the kinetics of the damage after the peak stress.

[Figure 8 about here]

The post-peak shape with a non-zero plateau is made possible thanks to the contribution of the second term (the term $-(1-A)\varepsilon_0/\varepsilon_{eq}^{max}$) in the damage evolution law (11)). For high strain levels, this contribution tends toward zero slower than the contribution with the exponential, so that when ε tends towards infinity:

$$D \underset{+\infty}{\sim} 1 - \frac{(1-A)\varepsilon_0}{\varepsilon}. \tag{13}$$

Thus, when putting equation (13) into equation (10), the stress tends towards a constant value $\sigma^{plateau}$, the value of the plateau in Figure 8.

$$\sigma \underset{\varepsilon \to +\infty}{\longrightarrow} (1-A)\varepsilon_0 E = \sigma^{plateau}. \tag{14}$$

4.2. A damage evolution law for the in-plane shearing of the woven composite material

The formalism of the Mazars model is now extended in order to describe the plateau of the pursued behavior for 3D woven composites (see Figure 7). Therefore, two evolution laws are mixed in an original manner:

- first, the ODM-type evolution law which evolves slowly, and is able to describe non-softening non-linearities,

- second, and after a threshold governed by the amount of in-plane shear, the Mazars-type evolution law which causes softening and presents a post-peak plateau.

Particular attention is therefore paid to the transition between both evolution laws. In order to ensure the continuity for any value of the damage and of its evolution rate, both ODM-PMC and Mazars damage evolution laws are written in a rate form, defined as , $\dot{D} = \frac{dD}{dt}$, and given by :

$$\dot{D} = \begin{cases} \dot{D}_{ODM} & \text{if } \mid \gamma_{12} \mid \leq \gamma_{12}^{S}, \\ \dot{D}_{Mazars} & \text{otherwise.} \end{cases} \tag{15}$$

The rate $\dot{D}_{ODM}$ (obtained by deriving D_{ODM}, reported in equation (8), with $\dot{d}_{ODM}$ corresponding to the derivative over time of the evolution law given by equation (5)) is given by:

$$\dot{D}_{ODM} = \frac{\dot{d}_{ODM}}{(1 + d_{ODM})^2} \tag{16}$$

$$\begin{cases} \dot{d}_{ODM} = (d^{sat} - d_{ODM}) \frac{s}{S} \left\langle \frac{\varepsilon_{eq} - \varepsilon_0}{S} \right\rangle^{s-1} \dot{\varepsilon}_{eq}^{max} \\ d_{ODM} = d^{sat} \left(1 - exp \left[- \left\langle \frac{\varepsilon_{eq}^{max} - \varepsilon_0}{S} \right\rangle^{s} \right] \right) \end{cases} \tag{17}$$

Instead of using the driving forces, the equivalent strain ε_{eq}, consistent with a strain and easier to be used by engineers in design office, is considered in the damage evolution law and is computed from the ODM-PMC driving forces (equation (2)) as:

$$\varepsilon_{eq_i} = \sqrt{\frac{2y_i}{C_{ii}^0}}, \qquad \text{(no sum) with } (i = 1, 2) \tag{18}$$

Nonetheless for readability matters, the index indicating the affected (degradation) direction ($i = 1$ or 2) is omitted here (for ε_{eq} as well as for D_{ODM} and d_{ODM}).

The maximum value ε_{eq}^{max} of ε_{eq} over the whole history, up to current time, is considered, so that damage can only increase, especially when the loading rises up to the last highest value, so that Kaiser effect can be ensured:

$$\varepsilon_{eq}^{max}(t) = \sup_{t \leq \tau} \varepsilon_{eq}(\tau) \quad \text{so that} \qquad \frac{d}{dt}\varepsilon_{eq}^{max} = \left\langle \frac{d}{dt}\varepsilon_{eq}^{max} \right\rangle \geq 0 \tag{19}$$

The rate $\frac{d}{dt}\varepsilon_{eq}^{max} = \dot{\varepsilon}_{eq}^{max}$ is the time derivative of this quantity and is used in equations (17). For each direction, 4 parameters are used: ε_0, S, s, d^{sat} for the ODM-type law, corresponding to respectively y_0, y_c, p and d^{sat} in equation (5).

The second phase of the behavior, described by the Mazars-type evolution law, is only relevant to in-plane shear loading. Hence, the switching between both evolution laws is defined here as a function of the amount of in-plane shear strain only (using the threshold γ_{12}^S expressed in equation (15)). The expression of the derivative evolution law associated to Mazars damage law ($\dot{D}_{Mazars}$) is given by:

$$\dot{D}_{Mazars} = \left[\frac{(1 - A - D_S)\varepsilon_{eq}^S}{\varepsilon_{eq}^2} + \frac{A}{S_c} \exp\left(- \left\langle \frac{\varepsilon_{eq} - \varepsilon_{eq}^S}{S_c} \right\rangle \right) \right] \dot{\varepsilon}_{eq}^{max} \tag{20}$$

Therefore, for each direction, 2 parameters A and S_c must be identified for the Mazars-type law, which correspond to A and $1/B$ in equation (11). The quantity ε_{eq}^S is not a parameter of the model but corresponds to the value of ε_{eq} at the transition between both laws (using the transition values of the strain tensor in equations (18) and (2)), which is loading dependent. Also,

$D_S = D(\varepsilon_{eq}^S)$ is the corresponding damage value of the damage D computed at the transition value of the equivalent strain ε_{eq}^S. It is worth pointing out that the proposed law (15) enforces the condition $D \underset{\varepsilon_{eq} \to +\infty}{\longrightarrow} 1$.

The sensitivity of the local behavior to the newly introduced model parameters A and S is shown in Figure 9. More precisely, we compute the sensitivity of the behavior to a new variable $\tau_{12}^{plateau}$ computed from A which directly corresponds to the stress value at the plateau:

$$\tau_{12}^{plateau} = G_{12}(1 - A - D_S)\varepsilon_{eq}^S. \tag{21}$$

The parameter $\tau_{12}^{plateau}$ also affects the damage evolution of the softening transition phase. The peak in the in-plane shear strain-stress curve is sharp for high values of $\tau_{12}^{plateau}$ while it gets smoother for lower values. The lower is the value of $\tau_{12}^{plateau}$, the more delayed is the peak from the threshold γ_{12}^S. The shape of the transition between the ODM-type damage law and the plateau is also affected by the parameter S_c that controls the evolution of the softening part of the model. The lower is the value of S_c, the more brutal is the transition. Thus, both parts of the model can easily be identified with the two law parameters $\tau_{12}^{plateau}$ and S_c.

[Figure 9 about here]

4.3. Summary of the model

The equations of the model can be summarized as follows. The effects of the damages are taken into account through the effective compliance tensor $\underline{\underline{S^{eff}}}$:

$$\boldsymbol{\sigma} = \underline{\underline{C}}^{eff} : \boldsymbol{\varepsilon}, \tag{22}$$

with:

$$(\underline{\underline{C}}^{eff})^{-1} = \underline{\underline{S}}^{eff} = \underline{\underline{S}}^{0} + \frac{D_1}{1-D_1}\underline{\underline{H}}_1 + \frac{D_2}{1-D_2}\underline{\underline{H}}_2, \tag{23}$$

where $\underline{\underline{S}}^{0}$ is the initial compliance of the material and the tensors $\underline{\underline{H}}_1$ and $\underline{\underline{H}}_2$ describe the effect of the damages in the warp and weft directions respectively. D_1 and D_2 are the corresponding damage variables that describe matrix cracking. Both variables evolve from 0 to 1. The evolution laws of the damage variable D_1 and D_2 are written in a rate form as follows:
If $\mid \gamma_{12} \mid \leq \gamma_{12}^{S}$, then

$$\dot{D}_i = \frac{\dot{d}_i}{(1+d_i)^2}, \text{ with } \dot{d}_i = (d_i^{sat} - d_i)\frac{s_i}{S_i}\left\langle \frac{\varepsilon_{eqi} - \varepsilon_{0i}}{S_i} \right\rangle^{s_i - 1} \dot{\varepsilon}_{eqi}^{max} \tag{24}$$

Otherwise, if $\mid \gamma_{12} \mid > \gamma_{12}^{S}$:

$$\dot{D}_i = \left[\frac{(1 - A_i - D_{Si})\varepsilon_{eqi}^{S}}{\varepsilon_{eqi}^{2}} + \frac{A_i}{S_{ci}} \exp\left(- \left\langle \frac{\varepsilon_{eqi} - \varepsilon_{eqi}^{S}}{S_{ci}} \right\rangle \right) \right] \dot{\varepsilon}_{eqi}^{max} \tag{25}$$

Each damage variable depends on 7 material parameters to be identified. For low in-plane shear strains ($\mid \gamma_{12} \mid \leq \gamma_{12}^{S}$), the evolution of the damage is governed by an ODM-type law. The values of the corresponding 4 parameters ε_{0i}, S_i, s_i, d_i^{sat} (with $i = 1, 2$) can be deduced from variables presented in section 3. For higher in-plane shear strains ($\mid \gamma_{12} \mid > \gamma_{12}^{S}$), the evolution of the damage switches to a Mazars-type law.

The 3 parameters that drive the evolution of the damage, A_i, S_{ci} and $\gamma^{S}{}_{12}$ cannot be identified easily on simple specimens, but only by inverse method on composite structures. The threshold γ_{12}^{S}, a material parameter, is set to the maximal shear strain measured by DIC at the beginning of the shear-out plateau. The parameters A_i and S_i as for them are identified, by trial and error, to match the experimental behavior with the simulation of the lug in

tension. To that end, the model is implemented into the Abaqus Standard FE software in Section 5.1, and a FE model of the lug is built in Section 5.2. The values of the parameters depend on the material direction due to the unbalanced ratio between the warp and weft tows. However in the following, for the sake of simplicity, identical values of A_i and S_i are used for both directions ($i = 1$ or 2). The material behavior obtained with the proposed model and identified parameters is illustrated in Figure 10. For reasons of industrial confidentiality, the values of the identified parameters are not provided.

[Figure 10 about here]

5. FE analysis of the shear-out failure of the 3D woven composite lug

5.1. Numerical implementation

The material model has been implemented as a UMAT in the Abaqus Standard finite element code. Special attention has been paid to the transition between the two evolution laws and the computation of the D_S and ε_{eq}^S quantities to avoid introducing any dependency on the discretization of the load. The behavior law is explicit with respect to the total strain. The local integration is explicit, which contributes to the overall efficiency and stability of the implementation. The tangent stiffness matrix has been checked for various multiaxial and non-proportional loading states to validate the model and minimize the computational times.

To avoid localization issues related to the softening damage, the Mazars-type evolution law is regularized by adding an artificial visco-damage effect

τ_i [35, 36, 37] in the damage evolution law:

$$\dot{D}_{v_i} = \frac{1}{\tau_i}(D_i - D_{v_i}). \tag{26}$$

where D_{v_i} corresponds to the regularized damage variable. In this work, the regulation parameter τ_i is considered as a numerical parameter in the case of quasi-static loading rates.

5.2. FE model

The Finite Element (FE) simulation is performed on the lug with the commercial FE software Abaqus Standard. To reduce the computational time, symmetry conditions are enforced to model an eighth of the lug only, as illustrated in Figure 11. The model comprises 29.226 linear hexaedric (C3D8) elements and 102.822 degrees of freedom. An analytical surface representative of a rigid axis, which is in contact with the boundary of the hole, is introduced in the model. In the simulation, a displacement is applied to the axis at a rate which is representative of the test. As a matter of simplicity, the friction coefficient is set here to 0. A region of the upper surface of the lug (shown in red in Figure 11) is blocked in the 3 directions. The corresponding area agrees with the clamping jaws area in contact with the lug.

[Figure 11 about here]

5.3. Results and discussion

The global load-displacement behavior is illustrated in Figure 12. The figure compares the results obtained using ODM-PMC, the proposed model and the experimental data. The responses of the two models are identical

in the first phases of the test. The first stages of the damage are correctly captured, although the non-linearity of the experimental curve is slightly underestimated before reaching the load plateau. The interest of the proposed damage model over the ODM-PMC becomes obvious for the description of the load plateau characteristic to the progressive and stable development of the shear-out failure of lug. The ODM-PMC underestimate the non linear response, while the proposed model describes a stable load plateau.

[Figure 12 about here]

Figures 13 and 14 illustrate the pattern of the damages D_1 and D_2 respectively. The damage patterns are given for four different values of the imposed displacement shown in Figure 12. The figures compare the damage patterns obtained with ODM-PMC and with the proposed model. At the instants (a) and (b), the patterns of the damage D_1 are rather similar with the two models. The damage D_1 develops itself along the shear-out plane, starting from the boundary of the hole. With the proposed model, the damage D_1 seems to be slightly ahead of the ODM-PMC damage, and the maximal values of D_1 is more localized along the shear-out plane.

However, the patterns of the damage D_2 are very dissimilar. Even if the global behaviors, depicted in Figure 12, seem to be similar with ODM-PMC and the proposed model until instant (a), we can see that the patterns of the damage D_2 are not similar at this time. These differences can be explained by the fact that, in the proposed model, the shear threshold associated to the Mazars evolution law is reached locally at some integration points, close to the hole. The stress distribution and then the damage patterns are therefore different.

At the instant (a), the ODM-PMC damage D_2 is already developed along the whole shear-out plane and reaches saturation in nearly half of the ligament. The evolution of the damage D_2 with the proposed model is much slower and can be followed step by step from instant (a) to instant (d). The damage develops steadily along the shear-out plane until crossing the whole ligament. During the global load plateau, the damage D_2 stays localized along the shear-out plane. Both damage variables reaches values close to 1 along the whole ligament, clearly indicating that the local Mazars plateau is reached at every integration point along the shear-out plane. The damages with ODM-PMC tend to spread in a much larger area and fail to reproduce the distinctive damage pattern of the shear-out failure.

It can be seen from Figure 13 that the damage D_1 also develops during the load plateau in the net section and behind the hole. The damage in the net section is due to the increasing longitudinal strains. The damage behind the hole is due to the global deformation of the lug that generates in-plane shear strains in this area.

It is clear from Figures 13 and 14 that the damage patterns in the simulations differ in both directions. In the present work, identical values of A_i and S_i are used for both directions ($i = 1$ or 2). This choice is arbitrary considering that the 3D-woven composite material used here is highly unbal-anced. Further work is needed to perform a more accurate identification of the model. Additionally, the only non-linear mechanisms that is considered in this paper is matrix damage. Thus, all the non-linearities observed for the off-axis 45°-test in Figure 6 and Figure 10 are due to the effect of the matrix damage. In particular, matrix viscoelasticity is neglected. Adding

viscoelasticity mechanisms to the model will also affect the identification of its parameters.

All in all, the proposed model could be used in design and analysis office for sizing lugs made of the same range of 3D woven composite material, with homothetic dimensions with respect to the presented lug. In such a configuration, shear-out remains the predominant failure mode. The proposed model should be therefore adapted to predict its failure. Attention must be paid to the modification of the hole diameter, which implies a change of lo-cal crack velocity. Hence the necessity to adjust the artificial visco-damage effect, and the model parameters that drive the damage evolution law.

Considering a lug -made of the same material- with any shape or size, there is a competition between the failure modes, namely shear-out, bearing and tension. The proposed model succeeded to model shear-out. It has been shown in past work that the ODM-PMC model was already well-tried to model bearing [38] and tension [39, 34]. Further work should be carried out to add the current modification on matrix cracking to the whole ODM-PMC model in order to have a model capable of predicting any mixed-mode failure of a 3D woven composite lug.

[Figure 13 about here]

[Figure 14 about here]

6. Conclusion

The shear-out failure mode for mechanically fastened joints can be critical for some specific applications. This is typically the case for monolithic 3D woven composite lugs. In this study, such a lug is tested up to failure. The

global load displacement curve exhibits a stable load plateau corresponding to the development of the shear-out failure. The failure is monitored using both digital image correlation and acoustic emission. X-ray tomography is performed after the test. The experimental data show that the shear-out failure is driven by the constant development of matrix damage along two parallel planes extending through the whole thickness from the hole boundary to the end of the lug.

A progressive damage model is proposed to describe the shear-out failure of the 3D woven composite lugs. This model is based on the Onera Damage Model for Polymer Matrix Composite (ODM-PMC), a continuum damage model developed for 3D-woven composites with polymer matrix. The ODM-PMC matrix damage evolution law is combined with a Mazars-type evolution law to describe a first non-softening damage phase for low in-plane shear strain values, followed by a short softening damage phase that ends with a stress plateau for high in-plane shear strain values. Specific attention is paid to the identification of the parameters of the damage law. The modified material model is implemented as a UMAT in Abaqus Standard. The model is applied to the detailed finite element analysis of the lug. The global behavior and the shear-out failure of the lug are successfully captured.

Further work is needed to introduce the matrix viscosity into the model and to describe the residual strains observed after unloading, that could be due to friction effects preventing the closure of the matrix cracks.

Acknowledgment

This research project results from a partnership between SAFRAN, ONERA and LMT. This work was supported under the PRC MecaComp, research project funded by DGAC and managed by SAFRAN.

A. Formulation of positive strains

The formulation of the positive strains $\boldsymbol{\varepsilon}^+$, for orthotropic materials in the present case, is based on the works of Ladevèze and Lemaitre [40], Ortiz [41], [42], and Ju [43] for initially isotropic materials. These authors defined the positive strain tensor $\boldsymbol{\varepsilon}^+$ as the positive part (using Macaulay brackets) of the total strain tensor in terms of principal value,

$$\boldsymbol{\varepsilon} = \sum_{I=1}^{3} \lambda_I \boldsymbol{e}_I \otimes \boldsymbol{e}_I, \qquad \boldsymbol{\varepsilon}^+ = \sum_{I=1}^{3} \langle \lambda_I \rangle \boldsymbol{e}_I \otimes \boldsymbol{e}_I \tag{27}$$

Thanks to the consideration of an initial orthotropy, such a definition has been modified [33, 34] to enable the calculation of the derivative of the positive strains and the tangent matrix of the model. A simplified positive strain is computed for each damage $(d_i, i = 1, 2)$ in the model, in the orthotropy basis. One defines a driving strain $\boldsymbol{\varepsilon}^{d_i}$ for each degradation mechanism, such as the only non zero strain components $(\boldsymbol{\varepsilon}^{d_i})_{ij}$ are those present in the corresponding driving force (see equation (2)). For instance, in the warp direction $(i = 1)$, driven by y_1, only strains ε_{11}, ε_{12}, and ε_{13} are considered, therefore $\varepsilon_{11}^{d_1} = \varepsilon_{11}$, $\varepsilon_{12}^{d_1} = \varepsilon_{21}^{d_1} = \varepsilon_{12}$, $\varepsilon_{13}^{d_1} = \varepsilon_{31}^{d_1} = \varepsilon_{13}$. The considered strain tensors are:

$$\boldsymbol{\varepsilon}^{d_1} = \begin{bmatrix} \varepsilon_{11} & \varepsilon_{12} & \varepsilon_{13} \\ \varepsilon_{12} & 0 & 0 \\ \varepsilon_{13} & 0 & 0 \end{bmatrix}, \qquad \boldsymbol{\varepsilon}^{d_2} = \begin{bmatrix} 0 & \varepsilon_{12} & 0 \\ \varepsilon_{12} & \varepsilon_{22} & \varepsilon_{32} \\ 0 & \varepsilon_{32} & 0 \end{bmatrix}. \tag{28}$$

This definition holds only in the orthotropy basis of the material.

Then, with this strain tensor $\boldsymbol{\varepsilon}^{d_i}$, the methodology proposed by Ladevèze-Lemaitre and others is applied, defining $(\boldsymbol{\varepsilon}^{d_i})^+$ as positive part —in terms of principal values, using equation (27)— of tensor $\boldsymbol{\varepsilon}^{d_i}$. A compacter notation is also proposed in the paper and used in equation (2) for the sake of readability, $(\boldsymbol{\varepsilon}^{d_i})^+$ is noted $\boldsymbol{\varepsilon}^{d_i+}$. After simplification, this leads to equations (29) and (30), for positive strain defined in the warp direction (damage d_1).

$$\boldsymbol{\varepsilon}^{d_1+} : \begin{cases} \varepsilon_{11}^{d_1+} = \frac{(\lambda_1)^3}{\Omega_1} \\ \varepsilon_{12}^{d_1+} = \frac{(\varepsilon_{12}\lambda_1)^2}{\Omega_1} \\ \varepsilon_{13}^{d_1+} = \frac{(\varepsilon_{13}\lambda_1)^2}{\Omega_1}, \end{cases} \tag{29}$$

where

$$\begin{gathered} \lambda_1 = \tfrac{1}{2}(\varepsilon_{11} + \sqrt{\varepsilon_{11}^2 + 4(\varepsilon_{12}^2 + \varepsilon_{13}^2)}), \\ \Omega_1 = \lambda_1^2 + (\varepsilon_{12}^2 + \varepsilon_{13}^2). \end{gathered} \tag{30}$$

and the same for $\boldsymbol{\varepsilon}^{d_2+}$.

This simplified formulation allows to derivate the positive strain with respect to the strain, and thus to analytically defined the tangent matrix. Also it is able to describe a reinforcement in compression and shear, with no additional parameters.

Data Availability

The raw data required to reproduce these findings cannot be shared at this time due to legal or ethical reasons. The processed data required to reproduce these findings cannot be shared at this time due to legal or ethical reasons.

References

[1] P. Camanho, M. Lambert, A design methodology for mechanically fastened joints in laminated composite materials, Composites Science and Technology 66 (15) (2006) 3004–3020. doi:10.1016/j.compscitech.2006.02.017.
URL http://linkinghub.elsevier.com/retrieve/pii/S0266353806000546

[2] G. Catalanotti, P. Camanho, P. Ghys, A. Marques, An efficient design method for multi-material bolted joints used in the railway industry, Composite Structures 94 (1) (2011) 246–252. doi:10.1016/j.compstruct.2011.06.018.
URL http://linkinghub.elsevier.com/retrieve/pii/S0263822311002388

[3] O. Gencoz, U. Goranson, R. Merrill, Application of finite element analysis techniques for predicting crack propagation in lugs, International Journal of Fatigue 2 (3) (1980) 121–129. doi:10.1016/0142-1123(80)90014-6.
URL https://linkinghub.elsevier.com/retrieve/pii/0142112380900146

[4] C. Kassapoglou, W. A. Townsend, Failure Prediction of Composite Lugs Under Axial Loads, AIAA Journal 41 (11) (2003) 2239–2243. doi:10.2514/2.6816.
URL http://arc.aiaa.org/doi/abs/10.2514/2.6816

[5] T. Collings, The strength of bolted joints in multi-directional cfrp laminates, Composites 8 (1) (1977) 43–55. doi:10.1016/0010-

4361(77)90027-1.
URL http://linkinghub.elsevier.com/retrieve/pii/0010436177900271

[6] L. J. Hart-Smith, Bolted Joints In Graphite-Epoxy Composites, Tech. rep., McDonnell Douglas Corp., Long Beach CA, Douglas Aircraft Div. (1976).

[7] P. Camanho, F. Matthews, Stress analysis and strength prediction of mechanically fastened joints in FRP: a review, Composites Part A: Applied Science and Manufacturing 28 (6) (1997) 529–547. doi:10.1016/S1359-835X(97)00004-3.
URL http://linkinghub.elsevier.com/retrieve/pii/S1359835X97000043

[8] Y. Xiao, T. Ishikawa, Bearing strength and failure behavior of bolted composite joints (part I: Experimental investigation), Composites Science and Technology 65 (7-8) (2005) 1022–1031. doi:10.1016/j.compscitech.2005.02.011.
URL http://linkinghub.elsevier.com/retrieve/pii/S0266353805000618

[9] J. Ekh, J. Schön, Finite element modeling and optimization of load transfer in multi-fastener joints using structural elements, Composite Structures 82 (2) (2008) 245–256. doi:10.1016/j.compstruct.2007.01.005.
URL https://linkinghub.elsevier.com/retrieve/pii/S0263822307000086

[10] S. D. Thoppul, J. Finegan, R. F. Gibson, Mechanics of mechanically fastened joints in polymer–matrix composite structures – A review, Composites Science and Technology 69 (3-4) (2009) 301–329.

doi:10.1016/j.compscitech.2008.09.037.
URL http://linkinghub.elsevier.com/retrieve/pii/S0266353808003862

[11] F.-X. Irisarri, F. Laurin, N. Carrere, J.-F. Maire, Progressive damage and failure of mechanically fastened joints in CFRP laminates – Part I: Refined Finite Element modelling of single-fastener joints, Composite Structures 94 (8) (2012) 2269–2277. doi:10.1016/j.compstruct.2011.07.023.
URL http://linkinghub.elsevier.com/retrieve/pii/S0263822311002820

[12] Y. Zhou, H. Yazdani Nezhad, C. Hou, X. Wan, C. McCarthy, M. McCarthy, A three dimensional implicit finite element damage model and its application to single-lap multi-bolt composite joints with variable clearance, Composite Structures 131 (2015) 1060–1072. doi:10.1016/j.compstruct.2015.06.073.
URL http://linkinghub.elsevier.com/retrieve/pii/S0263822315005371

[13] M. F. Wilhelm, U. Fuessel, T. Richter, M. Riemer, M. Foerster, Analysis of the shear-out failure mode for CFRP connections joined by forming, Journal of Composite Materials 49 (8) (2015) 981–993. doi:10.1177/0021998314528264.
URL http://journals.sagepub.com/doi/10.1177/0021998314528264

[14] M. McClain, N. Timoshchuk, Bearing behavior of 3d woven composites, Montreal, Canada, 2013, p. 8.

[15] K. C. Warren, R. A. Lopez-Anido, J. Goering, Behavior of three-dimensional woven carbon composites in single-bolt bearing, Composite

Structures 127 (2015) 175–184. doi:10.1016/j.compstruct.2015.03.022.
URL http://linkinghub.elsevier.com/retrieve/pii/S0263822315001944

[16] K. C. Warren, R. A. Lopez-Anido, S. S. Vel, H. H. Bayraktar, Progressive failure analysis of three-dimensional woven carbon composites in single-bolt, double-shear bearing, Composites Part B: Engineering 84 (2016) 266–276. doi:10.1016/j.compositesb.2015.08.082.
URL http://linkinghub.elsevier.com/retrieve/pii/S1359836815005223

[17] R. Mounien, C. Fagiano, P. Paulmier, B. Tranquart, F.-X. Irisarri, Experimental characterization of the bearing behavior of 3d woven composites, Composites Part B: Engineering 116 (2017) 369–376. doi:10.1016/j.compositesb.2016.10.077.
URL http://linkinghub.elsevier.com/retrieve/pii/S1359836816316444

[18] J. Lemaitre, J.-L. Chaboche, Mécanique des matériaux solides, Dunod, english translation 1990 'Mechanics of Solid Materials' Cambridge University Press, 1985.

[19] P. Ladeveze, E. Le Dantec, Damage modelling of the elementary ply for laminated composites, Composites Science and Technology 43 (3) (1992) 257–267.

[20] O. Allix, N. Bahlouli, C. Cluzel, L. Perret, Modelling and identification of temperature-dependent mechanical behaviour of the elementary ply in carbon/epoxy laminates, Composites Science and Technology 56 (7) (1996) 883–888.

[21] J. Lemaitre, R. Desmorat, Engineering Damage Mechanics : Ductile, Creep, Fatigue and Brittle Failures, Springer, 2005.

[22] J. W. Hutchinson, H. M. Jensen, Models of fiber debonding and pullout in brittle composites with friction, Mechanics of Materials 9 (2) (1990) 139–163.

[23] A. G. Evans, J. Domergue, E. Vagaggini, Methodology for relating the tensile constitutive behavior of ceramic-matrix composites to constituent properties, Journal of the American Ceramic Society 77 (6) (1994) 1425–1435.

[24] A. Burr, F. Hild, F. Leckie, Continuum description of damage in ceramic-matrix composites, European Journal of Mechanics - A/Solids 16 (1) (1997) 53–78.

[25] R. Gutkin, S. Costa, R. Olsson, A physically based model for kink-band growth and longitudinal crushing of composites under 3D stress states accounting for friction, Composites Science and Technology 135 (2016) 39–45. doi:10.1016/j.compscitech.2016.09.002.
URL https://linkinghub.elsevier.com/retrieve/pii/S0266353816311332

[26] C. Fagiano, M. Genet, E. Baranger, P. Ladevèze, Computational geometrical and mechanical modeling of woven ceramic composites at the mesoscale, Composite Structures 112 (2014) 146–156.

[27] G. Herrmann, J. Kestin, On the thermodynamics foundation of a damage theory in elastic solids, J. Mazars and Z.P. Bazant eds, Elsevier Amsterdam, 1988, Ch. Cracking and Damage, pp. 228–232.

[28] F. Ramtani, Y. Berthaud, J. Mazars, Orthotropic behavior of concrete with directional aspects: modelling and experiments, Nuclear Engineering Design 133 (1992) 97–111.

[29] J. Mazars, A description of micro- and macroscale damage of concrete structures, Engineering Fracture Mechanics 25 (5/6) (1986) 729–737.

[30] Vic-3D 7 Manual - Support.
URL http://www.correlatedsolutions.com/supportcontent/Vic-3D-v7-Manual.pdf

[31] A. Hurmane, F.-X. Irisarri, F. Laurin, S. Leclercq, M. Benzeggagh, Analyse de la tenue d'éprouvettes trouées composites tissées 3d sous sollicitations de compression au moyen d'un dialogue essais/calculs, Matériaux & Techniques 104 (4) (2016) 403. doi:10.1051/mattech/2016034.
URL http://www.mattech-journal.org/10.1051/mattech/2016034

[32] A. Elias, F. Laurin, M. Kaminski, L. Gornet, Experimental and numerical investigations of low energy/velocity impact damage generated in 3d woven composite with polymer matrix, Composite Structures 159 (2017) 228–239. doi:10.1016/j.compstruct.2016.09.077.
URL https://linkinghub.elsevier.com/retrieve/pii/S0263822316319729

[33] E. Hemon, Modèles multi-niveaux de prévision des durées de vie en fatigue des structures composites à matrice céramique pour usage en turbomachines aéronautiques, Doctorate thesis, Université Sciences et Technologies-Bordeaux I (2013).

[34] C. Rakotoarisoa, Prévision de la durée de vie en fatigue des compos-

ites à matrice organique tissés interlock, Doctorate thesis, Université de Technologie de Compiègne (2014).

[35] J.-F. Dubé, G. Pijaudier-Cabot, C. La Borderie, Rate Dependent Damage Model for Concrete in Dynamics, Journal of Engineering Mechanics 122 (10) (1996) 939–947. doi:10.1061/(ASCE)0733-9399(1996)122:10(939).
URL https://ascelibrary.org/doi/abs/10.1061/(ASCE)0733-9399(1996)122:10(939)

[36] P. Ladevèze, O. Allix, J.-F. Deü, D. Lévêque, A mesomodel for localisation and damage computation in laminates, Computer Methods in Applied Mechanics and Engineering 183 (1-2) (2000) 105–122. doi:10.1016/S0045-7825(99)00214-5.
URL http://linkinghub.elsevier.com/retrieve/pii/S0045782599002145

[37] A. Suffis, T. A. Lubrecht, A. Combescure, Damage model with delay effect, International Journal of Solids and Structures 40 (13-14) (2003) 3463–3476. doi:10.1016/S0020-7683(03)00153-7.
URL http://linkinghub.elsevier.com/retrieve/pii/S0020768303001537

[38] R. Mounien, Analyse expérimentale 3D et modélisation de la tenue et du comportement au matage de structures composites tissées 3D, Doctorate thesis, Université de Bretagne Occidentale (2017).

[39] L. Marcin, Modélisation du comportement, de l'endommagement, et de la rupture des matériaux composites à renforts tissés pour le dimensionnement robuste de structures, Doctorate thesis, Université de Bordeaux I (2010).

[40] P. Ladevèze, J. Lemaitre, Damage effective stress in quasi-unilateral condition, in: Proc. IUTAM Congress, Lyngby, Danemark, 1984.

[41] M. Ortiz, A constitutive theory for the inelastic behavior of concrete, Mechanics of Materials 4 (1985) 67–93.

[42] J. Simo, J. Ju, Strain- and stress-based continuum damage models—II. Computational aspects, International Journal of Solids and Structures 23 (7) (1987) 841–869. doi:10.1016/0020-7683(87)90084-9.
URL http://linkinghub.elsevier.com/retrieve/pii/0020768387900849

[43] J. Ju, On energy-based coupled elastoplastic damage theories: Constitutive modeling and computational aspects, International Journal of Solids and Structures 25 (7) (1989) 803–833. doi:10.1016/0020-7683(89)90015-2.
URL https://linkinghub.elsevier.com/retrieve/pii/0020768389900152

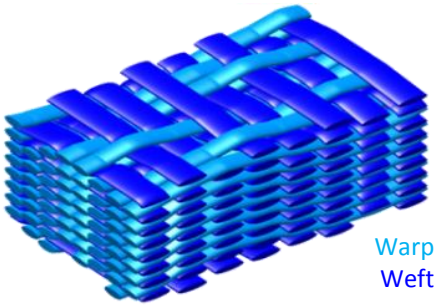

Figure 1: Example of an architecture of a 3D woven composite material

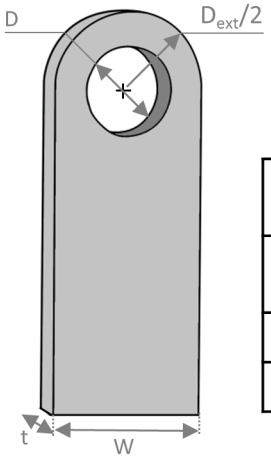

Hole diameter D (mm)	50
Outer diameter D_{ext} (mm)	75
Width (mm)	150
Thickness (mm)	19.6

Figure 2: Characteristic dimensions of the tested lug

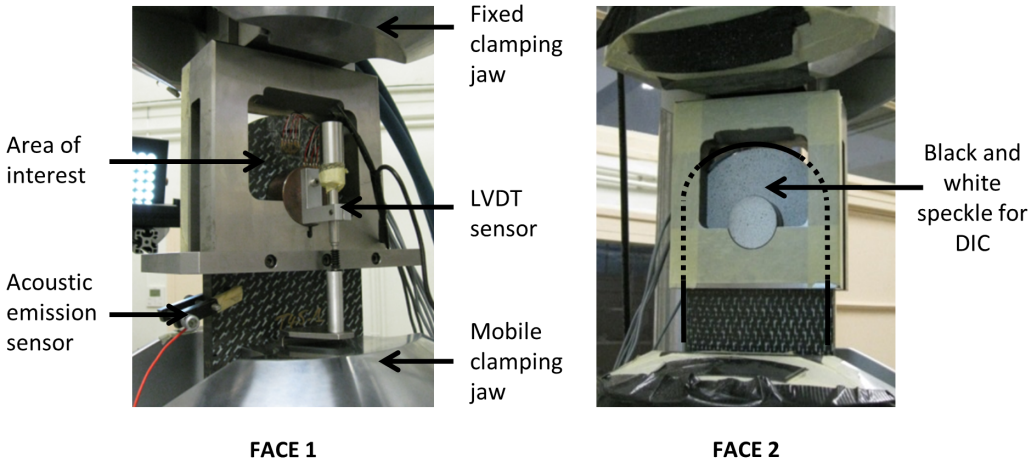

Figure 3: Experimental set-up

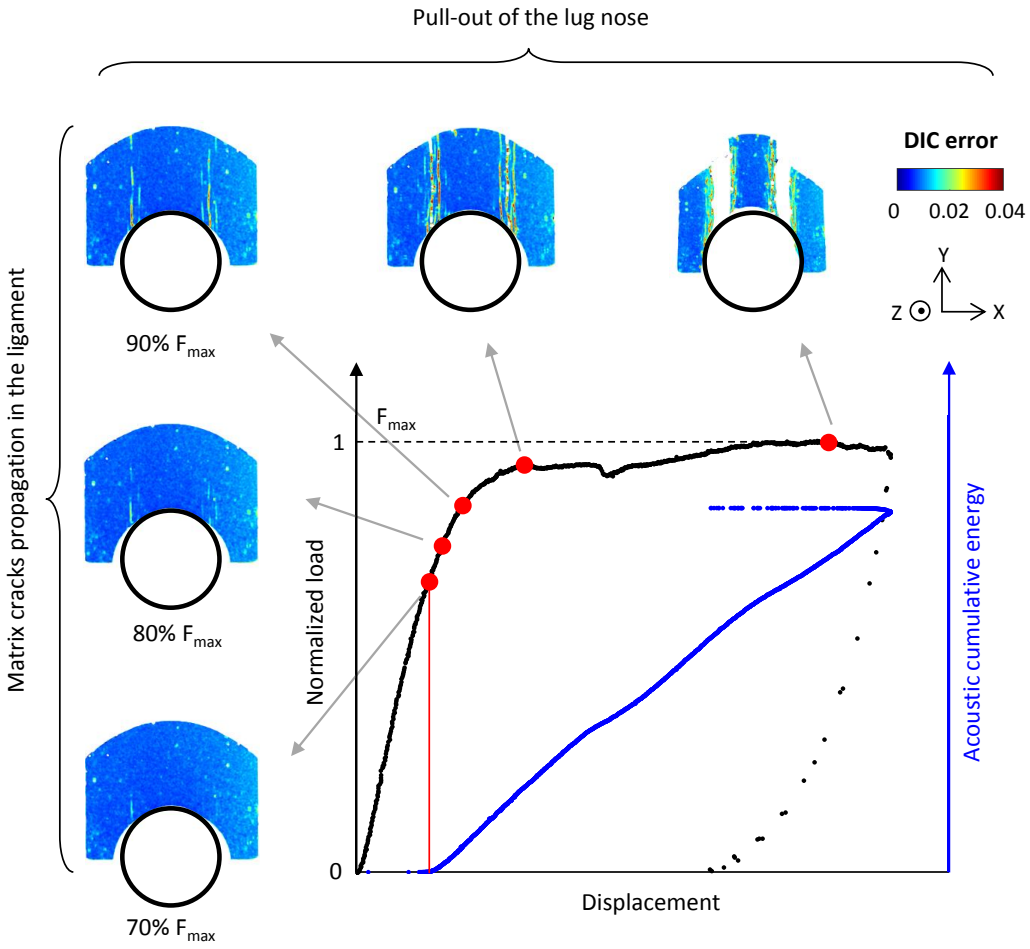

Figure 4: Global load/displacement response of the lug and cumulative acoustic emission energy. The DIC epipolar error is shown at different instants of the test with a magnification factor of 5 on the deformation of lug

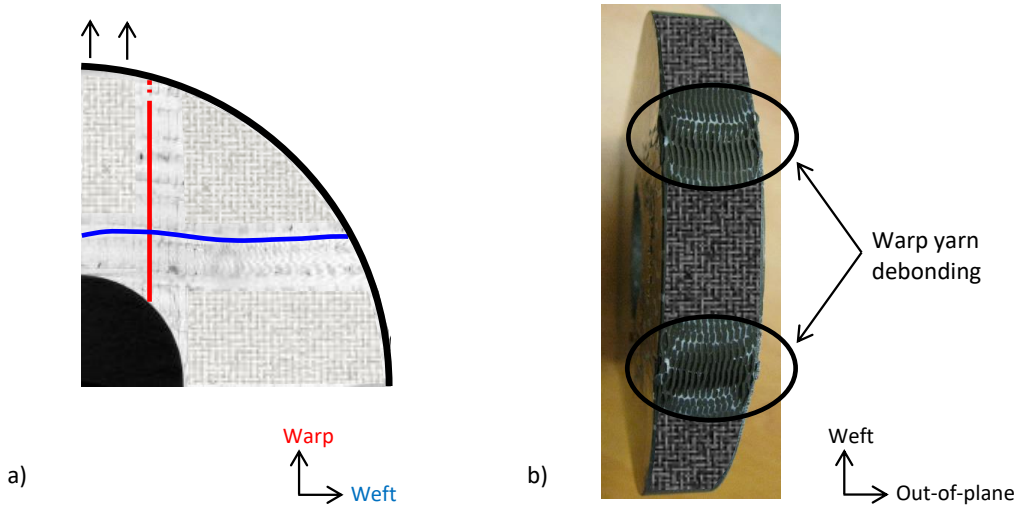

Figure 5: a) Observation of the shear-out damage pattern at the mid-thickness of the specimen using X-Ray tomography. b) Post-mortem picture of the yarn debonding at the extremity of the lug after the shear-out test

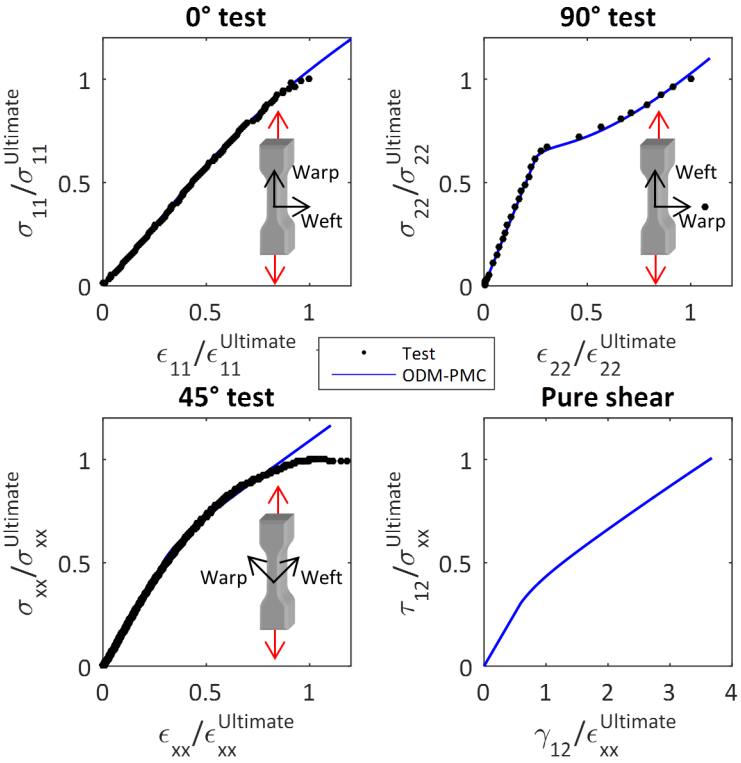

Figure 6: Comparison of the test data and the predicted behavior with ODM-PMC for the 0°tensile test, the 90°tensile test and the 45°tensile test, and pure in-plane shear behavior

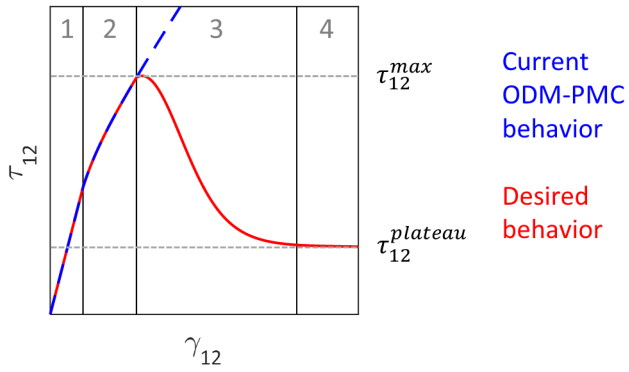

Figure 7: Shape of the desired local behavior under pure in-plane shear loading. Phase 1: linear behavior. Phase 2: damage onset and evolution for low shear strain values. Phase 3: softening transition phase. Phase 4: stress plateau for high shear strain values

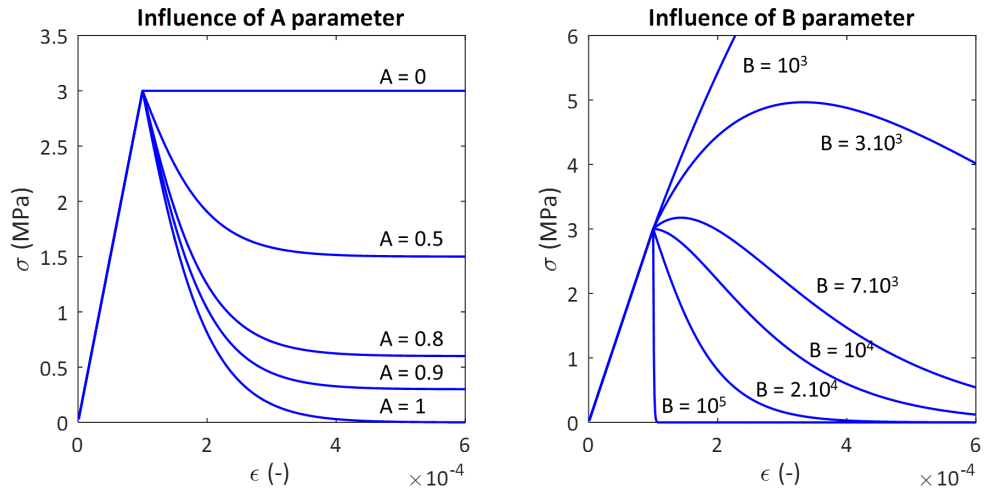

Figure 8: Sensitivity of the Mazars model (equation (11)) to the parameters A and B [29]

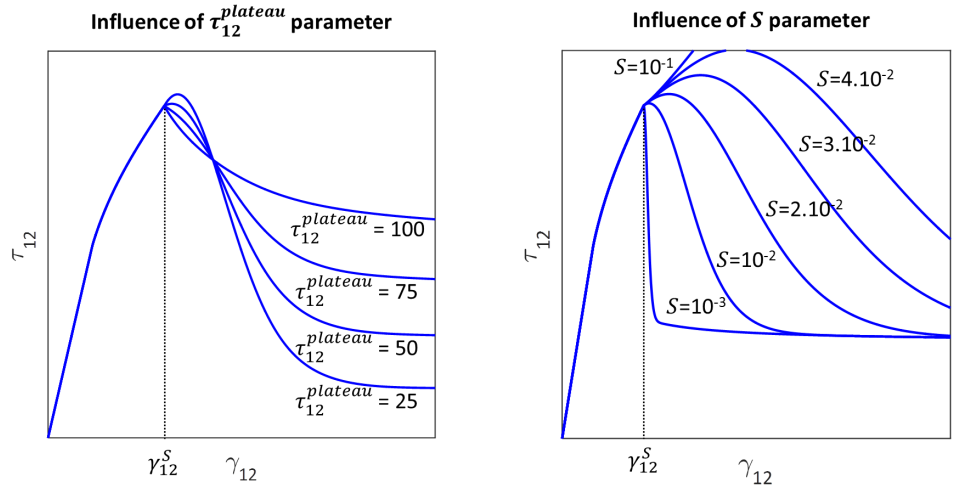

Figure 9: Sensitivity of the proposed model (equation (15)) to the parameters $\tau_{12}^{plateau}$ and S for a pure in-plane shear loading

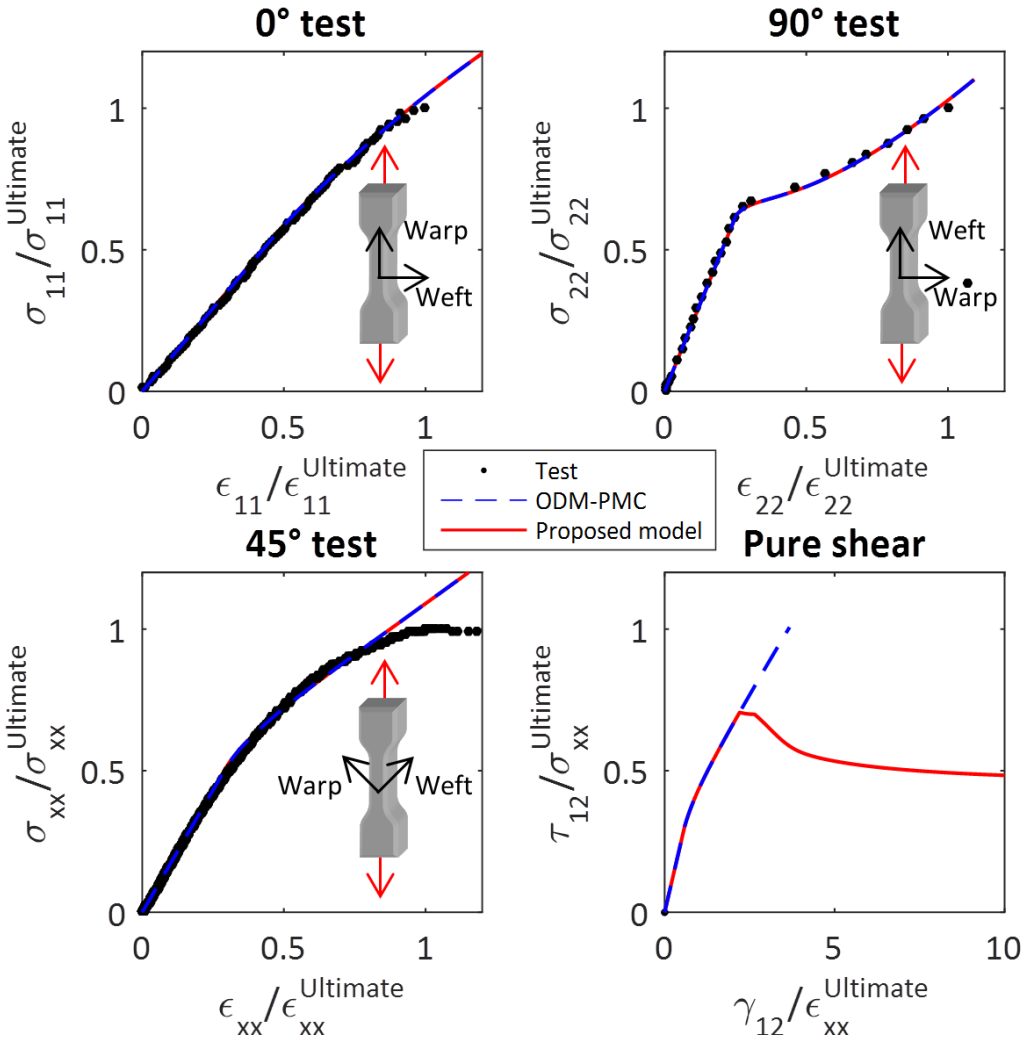

Figure 10: Comparison of the test data and the predicted behavior with ODM-PMC and the proposed model for the 0°tensile test, the 90°tensile test and the 45°tensile test, and pure in-plane shear behavior

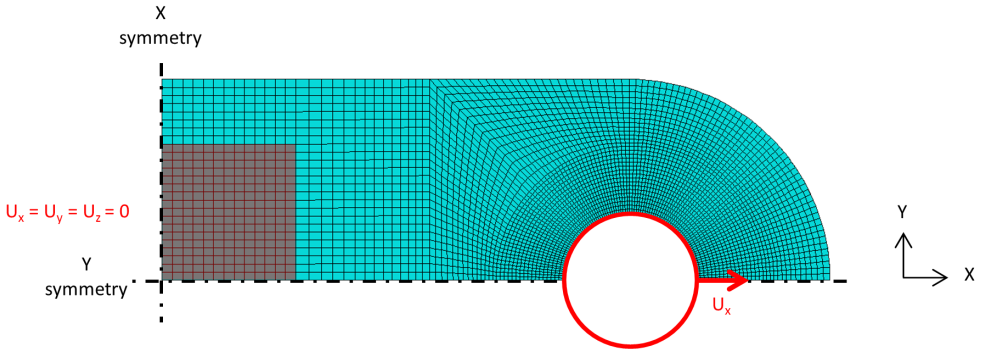

Figure 11: FE mesh of the lug and boundary conditions

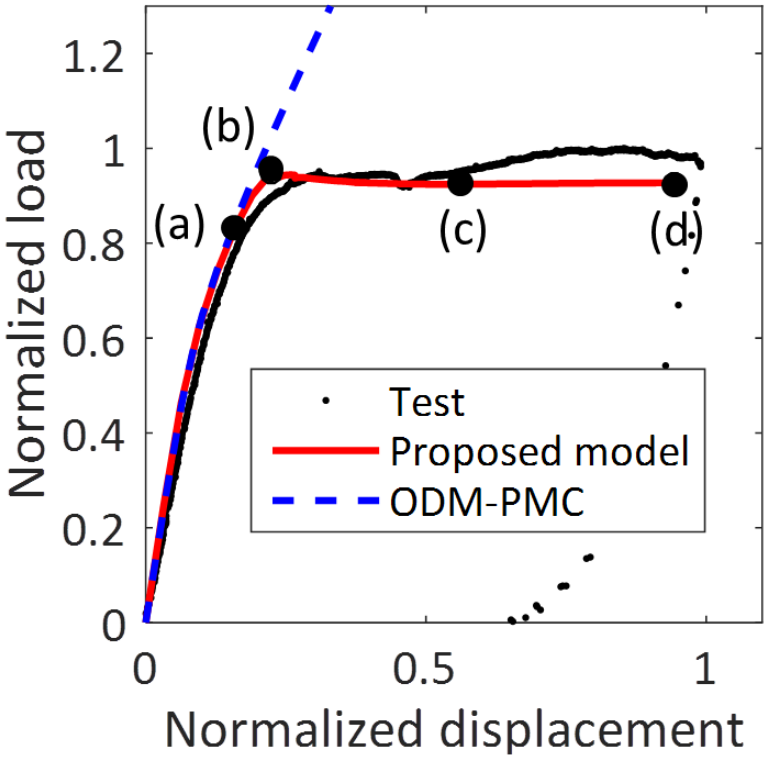

Figure 12: Comparison of the global load/displacement curves of the lug obtained with ODM-PMC, the proposed model and the test results

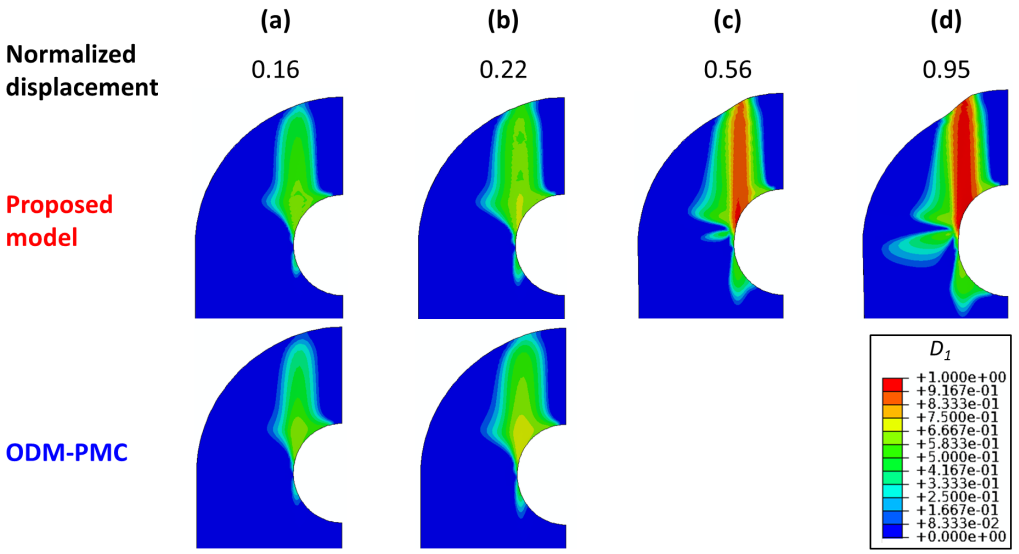

Figure 13: Pattern of the D_1 damage variable at different displacements defined in Figure 12 (displacements magnification factor: 2)

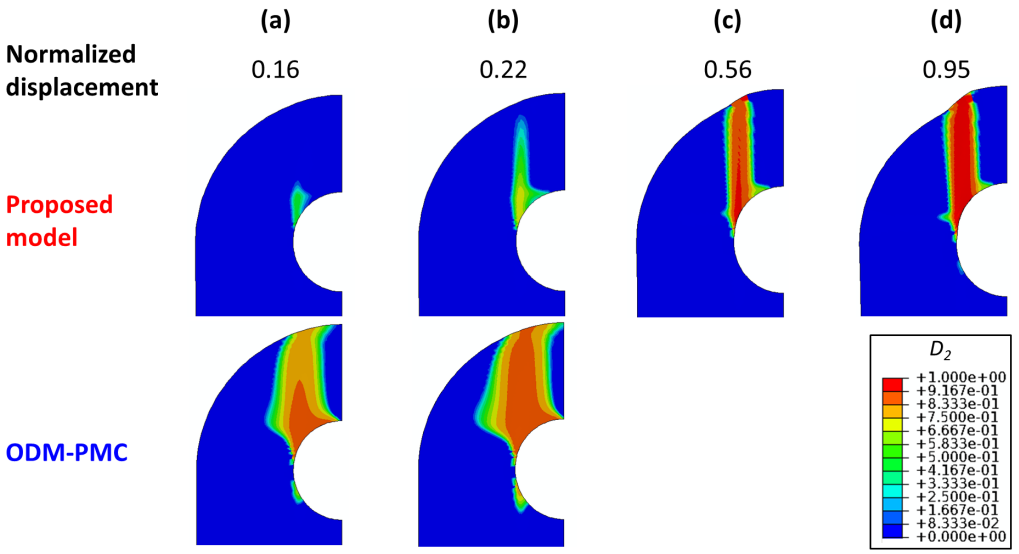

Figure 14: Pattern of the D_2 damage variable at different displacements defined in Figure 12 (displacements magnification factor: 2)